Korean Journal of Chemical Engineering (2024) 41:435–444
https://doi.org/10.1007/s11814-024-00015-6

ORIGINAL ARTICLE

Synthesis of Fe–MOF/COF Hybrid Materials for Methane Adsorption Using Design of Experiments

Min Hyung Lee[1] · Sangmin Lee[2] · Kye Sang Yoo[1,2]

Received: 30 August 2023 / Revised: 15 December 2023 / Accepted: 5 January 2024 / Published online: 10 February 2024

Abstract

This study focuses on the synthesis of Fe–MOF/COF (metal–organic framework/covalent organic framework) materials for methane adsorption. The synthesis process involves several steps, starting with the preparation of MIL-100(Fe) through the reaction of trimesic acid and iron(III) nitrate nonahydrate. MIL-100(Fe)_NH_2 is then synthesized by combining MIL-100(Fe) with ethylenediamine, followed by the synthesis of MIL-100(Fe)/COF through the addition of melamine, terephthalaldehyde, and dimethylsulfoxide. A definitive screening design and mixture method are employed to optimize the synthesis process by determining the influential factors and their respective ratios. The nitrogen content of samples is used as the response variable, and the optimized precursor molar ratio for MIL-100(Fe)/COF synthesis is estimated. From the main effect plots, TPA has the lowest effect on the response. The estimated actual precursor ratio for the optimized synthesis of MIL-100(Fe)/COF is MIL-100(Fe)_NH_2:TPA:MEL:DMSO:DIW = 1 mol:13 mol:10 mol:1884 mol:1648 mol. For the methane adsorption, the response optimizer indicated that MIL-100(Fe)/COF synthesized with a modified molar ratio of 0.1:0.4:0.5 (MEL:DMSO:DIW) was expected to exhibit the highest value.

Keywords Fe–MOF · COF hybrid · Toluene adsorption · Design of experiments · Optimization

Introduction

Methane adsorption, the process of capturing and storing methane molecules onto a solid material, has gained significant interest in recent years due to its relevance in energy storage, natural gas purification, and environmental sustainability. Methane, as the primary component of natural gas and a potent greenhouse gas, presents both economic and environmental challenges [1, 2]. Efficient and selective methane adsorption materials are crucial for its storage, transportation, and utilization. The development of advanced materials for methane adsorption has been driven by the need for efficient energy storage and the mitigation of methane emissions. These materials are designed to possess high methane uptake capacities, strong adsorption affinities, and excellent selectivity towards methane molecules. By adsorbing methane onto solid substrates, it can be effectively stored at lower pressures and higher densities, enabling more practical and economical storage solutions. Various classes of materials have been explored for methane adsorption, including porous materials such as MOFs, activated carbons, zeolites, and porous polymers [3–9]. These materials exhibit unique structural features, such as high surface areas, well-defined pore sizes, and tailored surface chemistries, which allow for efficient methane capture.

Iron-based metal–organic frameworks (Fe–MOFs) have emerged as a fascinating class of materials with remarkable properties and diverse applications. Fe–MOFs are a specific subset of MOFs in which iron ions or clusters are incorporated into the framework structure along with organic ligands. These materials exhibit a unique combination of characteristics, including high porosity, tunable pore size, and exceptional chemical stability [10–12]. The incorporation of iron in Fe–MOFs imparts additional functionalities such as redox activity, magnetic properties, and catalytic capabilities, expanding their potential applications in various fields [13–15]. Fe–MOFs offer a large surface area and

✉ Kye Sang Yoo
kyoo@seoultech.ac.kr

[1] Department of Energy and Chemical Engineering, Graduate School of Convergence Science, Seoul National University of Science and Technology, Seoul 01811, Korea

[2] Department of Chemical and Biomolecular Engineering, Seoul National University of Science and Technology, Seoul 01811, Korea

pore volume, providing ample space for guest molecules adsorption, gas storage, and separation processes. Their porous nature allows for precise control over pore size and shape, enabling selective adsorption and separation of specific target molecules. This feature makes Fe–MOFs highly desirable for applications such as gas storage, carbon capture, and purification of gases and liquids. Fe–MOFs can be synthesized through different methods, including solvothermal and hydrothermal synthesis techniques. One prominent member of the Fe–MOF family, MIL-100(Fe), has garnered significant attention due to its extensive investigation and promising prospects across various applications [16–18]. MIL-100(Fe) has demonstrated exceptional capabilities in gas adsorption, particularly for molecules such as carbon dioxide, hydrogen, and methane. Its outstanding performance in capturing and storing these gases makes it an attractive candidate for applications related to gas separation, storage, and environmental sustainability.

Recently, MOFs and COFs have garnered significant attention due to their distinct characteristics and wide-ranging potential applications across various fields [19]. MOFs consist of metal ions or clusters interconnected by organic ligands, resulting in a three-dimensional framework with a substantial surface area and pore volume [20–23]. Conversely, COFs are comprised of organic molecules linked together through covalent bonds, yielding a crystalline structure with precisely defined pores [24, 25]. Both MOFs and COFs have demonstrated promising capabilities in diverse areas such as gas storage and separation, catalysis, sensing, and drug delivery [26–29]. Moreover, in the context of sustainable development, researchers are actively exploring the capacity of MOFs and COFs to address environmental challenges like carbon capture and water purification.

Enhancing the synthesis process of Fe–MOF/COF materials to facilitate their commercial viability as effective adsorbents across various industries holds significant promise. Nevertheless, the optimization of the synthesis process presents a considerable challenge due to the diverse nature of Fe–MOF/COF and the growing complexity of involved precursors. Conventional trial and methods face drawbacks in terms of time and cost, demanding a large number of experiments. To address these challenges, leveraging appropriate statistical Design of Experiments (DOE) emerges as a promising solution. This involves tailoring an experimental method to specific objectives and planning experiments strategically to extract maximum information with minimal trials through statistical analysis and data processing. Various DOE methods, such as factorial, response surface, mixture, and Taguchi methods, have been developed [30–34]. While conventional DOE methods have traditionally been employed for simple process analysis or quality control in industrial settings, recent advancements have extended their application to analyze and optimize complex processes. Sequential designs of experiments enable the systematic selection of crucial factors and their optimization, providing a more efficient and insightful approach.

In this study, two consecutive Design of Experiments (DOE) methodologies were implemented to assess the synthesis processes of MIL-100(Fe)/COF. Initially, a screening method was employed to identify significant precursors for the synthesis. Subsequently, a mixture method was applied to optimize the ratios of these precursors. The outcomes of the DOE analysis were corroborated through methane adsorption, confirming the efficacy of the proposed approach. By incorporating statistical DOE methods into the optimization of MIL-100(Fe)/COF synthesis, this study seeks to overcome the limitations associated with traditional trial-and-error approaches. The integration of DOE not only alleviates the research burden related to optimization but also yields informative results for achieving synthesis processes that are both efficient and cost-effective. The successful optimization of MIL-100(Fe)/COF synthesis holds substantial promise for their extensive utilization as valuable adsorbents across diverse industries.

Experimental

MIL-100(Fe)/COF Synthesis

Trimesic acid, iron(III) nitrate nonahydrate, distilled water, ethylenediamine, melamine (MEL), terephthalaldehyde (TPA), and dimethylsulfoxide (DMSO) were procured from Sigma-Aldrich. Ethanol was obtained from Samjeon Chemical (Korea). These chemicals were used without any further purification. Trimesic acid and iron(III) nitrate nonahydrate were added to distilled water and stirred for 10 min. The molar ratio of precursors is 0.42:0.27:0.32. The resulting mixture was then transferred to autoclave and reacted at 160 °C and 12 h. Subsequently, MIL-100(Fe) was obtained by filtering the mixture solution, followed by washing with distilled water and ethanol. The obtained material was dried at 80 °C in oven. For preparation of MIL-100(Fe)_NH_2, MIL-100(Fe), ethylenediamine, and ethanol were added in a round-bottom flask. The mixture underwent a reflux reaction at 80 °C for 12 h while being mixed using a heated magnetic stirrer. The resulting mixture was filtered, washed with ethanol, and dried at 80 °C to obtain MIL-100(Fe)_NH_2. After, MIL-100(Fe)_NH_2, melamine, terephthalaldehyde, dimethylsulfoxide, and distilled water were stirred for 10 min. The amount of each reagent was adjusted according to the concentration ratio determined by the design methods. The mixture was then transferred to autoclave and reacted in an oven at 180 °C for 12 h. After the reaction, the final product was obtained by filtration, followed by washing with ethanol, and drying at room temperature, resulting in

the formation of MIL-100(Fe)/COF material. The chemical structure of MOF/COF is a reticular structure consisting of $C_3N_3H_6$ rings from melamine and benzene from terephthaladehyde covalently bonded to MIL-100 with N as the bridge.

Characterization

The materials were characterized using a powder X-ray diffractometer (Shimadzu XRD-6000, Japan) operating at 40 kV and 30 mA with Cu Kα ($\lambda = 0.15418$ nm) radiation to determine the crystal structure and crystallinity. Fourier transform infrared spectra were measured using an infrared spectrometer (Thermo Fisher Scientific iS50, USA), covering a range of 4000 to 400 cm^{-1}. The samples were mixed with KBr to form pellets for the measurements. The sample images were confirmed using scanning electron microscopy (JEOL, JSM-6700 F). The C, H, N, S elemental analysis of the sample was performed at 950 °C using a Thermo Scientific elemental analyzer (FLASH EA 1112, USA) with sulfamethazine (C: 51.8%, H: 5.1%, N: 20.1%, S: 11.5%) as a standard.

Design of Experiments

All statistical analyses were conducted using Minitab 21 software. The Assistant DOE comprises a subset of the DOE features found in the core Minitab, employing a sequential experimentation approach that streamlines the creation and analysis of designs. It initiates by screening designs to pinpoint crucial factors. Subsequently, more detailed designs are introduced to detect curvature and establish a conclusive model for identifying optimal factor settings that optimize the response.

Methane Adsorption

Prior to methane adsorption, the adsorbent sample underwent activation in a helium atmosphere at 150 °C for 2 h. The methane breakthrough test was conducted using a stainless-steel tube at 1 atm and 3 atm. In each experimental run, 20 mg of the adsorbent was loaded into the bed. Methane gas, with a balanced air concentration of 1000 ppm (0.1%), was passed through the fixed bed at a flow rate of 100 mL/min. Gas chromatography (YL6500GC, Younglin Co., Ltd., Korea) equipped with flame ionization detectors was used to analyze the toluene. The column used was BR-5 (Bruker, capillary 30 m × 0.25 mm), and the oven temperature was maintained at 200 °C throughout the analysis. Breakthrough curves were used to investigate the performance of the adsorbent for methane. The adsorption capacity (q) was calculated as the total mass of toluene adsorbed (mg/g) per unit weight of MIL-100/COF. It was calculated by the following formula:

$$q = \frac{QC_{\text{in}}}{m}\int_0^{t_s}\left(1 - \frac{C_{\text{out}}}{C_{in}}\right)\mathrm{d}t,$$

where C_{in} and C_{out} were influent and effluent concentrations of methane (mg/m^3). Q was the volumetric flow rate (m^3/min), m was the total mass of MIL-100/COF (mg) and t_s (min) was the time to reach saturation.

Results and Discussion

Characterization

Figure 1a displays the XRD patterns for both the MIL-100(Fe) synthesized in this study and the theoretical MIL-100(Fe). The XRD analysis reveals that the experimentally synthesized MIL-100(Fe) exhibits peaks ($2\theta = 4.91°$, 6.00°, 6.35°, 6.90°, 10.31°, 11.07°, 12.62°, 14.32°, 20.17°, 24.18°) that align with the theoretically calculated peaks. This result confirms the successful formation of well-defined Fe–MOF crystals [36]. The XRD patterns for MIL-100(Fe)_NH_2 and MIL-100(Fe)@COF are illustrated in Fig. 1b. It is evident that the crystallinity of both MIL-100(Fe)_NH_2 and MIL-100(Fe)@COF lacks distinct peaks compared to MIL-100(Fe). In the XRD pattern of MIL-100(Fe)_NH_2, peaks are detected around 8° and 11°, while a peak is formed around 21° in the XRD pattern of MIL-100(Fe)@COF. The result is probably related to the overlap of XRD peaks of MIL-100(Fe) and MIL-100(Fe)@COF, and the corresponding COF and MOF peaks were well observed with short tentacles and wide spikes.

Figure 2 illustrates the FT-IR spectra of the MIL-100(Fe), MIL-100(Fe)_NH_2 and MIL-100(Fe)/COF samples, providing experimental evidence for the bonding of the synthesized materials. In the FT-IR spectrum of MIL-100(Fe), several spectral peaks can be observed. The peaks at 3380 cm^{-1} indicate the O–H stretching vibration of the adsorbed water molecules, while the peak at 1704 cm^{-1} corresponds to the C=O bond of the unreacted raw material BTC [35]. Additionally, the asymmetric stretching vibrations of COO– are visible at 1625 and 1571 cm^{-1}, and the symmetric stretching vibrations of COO– are observed at 1442 and 1371 cm^{-1}. These peaks indicate the presence of COO– groups [35]. Furthermore, the bending vibration of the C–H bond in the benzene ring is identified at 760 and 711 cm^{-1}, and the stretching vibration of Fe–O is detected at 484 cm^{-1} [35]. In the FT-IR graph of MIL-100(Fe)_NH_2, a new spectral peak is observed in the range of 3250–3300 cm^{-1}, indicating the stretching vibration of N–H originating from the amino group. The C–H stretching vibration of ethylenediamine (EDA) is identified at 2942 cm^{-1}. Furthermore, C–N stretching vibrations are visible at 1350 cm^{-1} and 1200 cm^{-1}, and a bending vibration peak of N–H is observed at 815 cm^{-1}.

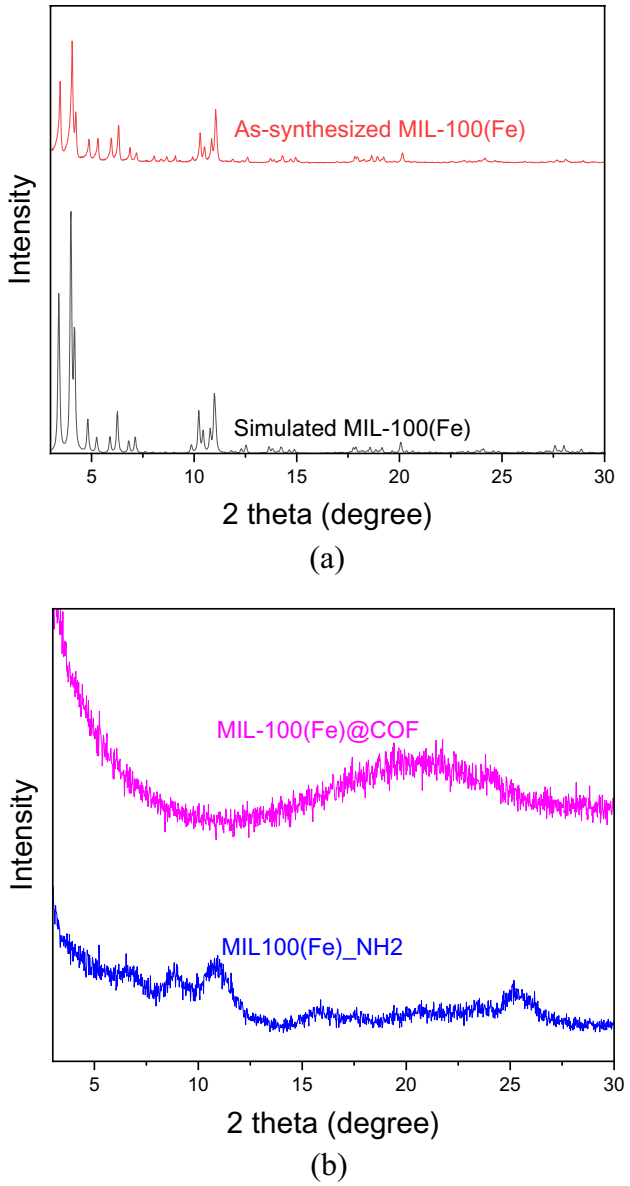

Fig. 1 XRD patterns of **a** simulated and as-synthesized MOF-100(Fe) and **b** MIL-100(Fe)_NH_2 and MOF-100(Fe)/COF

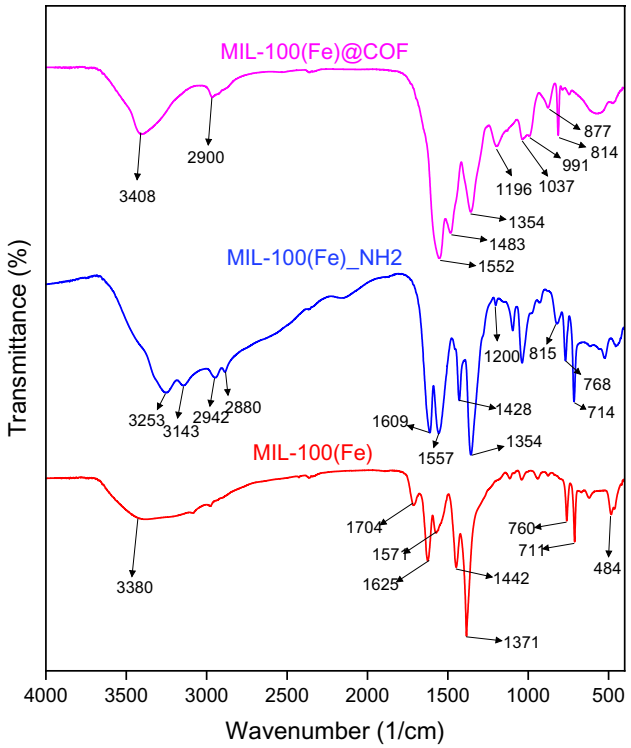

Fig. 2 FT-IR spectra of MOF-100(Fe), MIL-100(Fe)_NH_2 and MOF-100(Fe)/COF

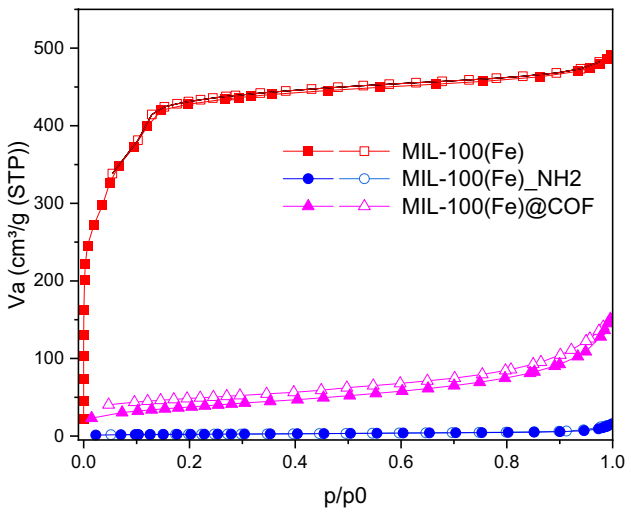

Fig. 3 N_2 adsorption–desorption isotherms of MOF-100(Fe), MIL-100(Fe)_NH_2 and MOF-100(Fe)/COF (closed symbol: adsorption, open symbol: desorption)

These findings suggest that EDA is grafted on the surface of MIL-100(Fe). The presence of these peaks confirms the bonding interactions [35–37]. In the FT-IR spectrum of MIL-100(Fe)/COF, distinctive peaks can be observed. The N–H stretching vibration peak is identified at 3408 cm^{-1}, and the C–H stretching vibration is observed at 2900 cm^{-1}. Additionally, the C=N, C=C, and C–N bonds are detected at 1552, 1483, and 1354 cm^{-1}, respectively [36]. A characteristic peak of C–N stretching vibration is observed at 1196 cm^{-1}. The bending vibration of N–H is also identified at 814 cm^{-1}. The FT-IR analysis confirms the existence of C–N and C=N bonds in MIL-100(Fe)/COF, and the nitrogen content of the sample is subsequently used as a reaction response in the experimental plan for optimizing the synthesis of MIL-100(Fe)/COF.

The isotherm graph obtained from nitrogen adsorption and desorption measurements was presented in Fig. 3 to evaluate the structural properties of the synthesized sample.

The isotherm curve of MIL-100(Fe) exhibited type I behavior, which is commonly observed in adsorption processes governed primarily by physical forces like van der Waals interactions. This type of isotherm is frequently observed in microporous materials such as activated carbon, zeolites, and specific MOFs. On the other hand, MIL-100(Fe)/COF displayed a type II isotherm curve, indicating unrestricted monolayer–multilayer adsorption. The arrow marking the commencement of the nearly linear middle section of the isotherm often indicates the completion of monolayer coverage and the onset of multilayer adsorption. This characterization provides valuable insights into the properties of the two substances. The MIL-100(Fe) sample displayed a BET surface area of 1068 m^2/g and a pore volume of 0.76 cm^3/g. In contrast, MIL-100(Fe)_NH_2 showed a significantly reduced BET surface area of 16 m^2/g and a much smaller pore volume of 0.003 cm^3/g. On the other hand, MIL-100(Fe)/COF exhibited an increased BET surface area of 220 m^2/g and a larger pore volume of 0.36 cm^3/g due to the formation of COF structure.

FE-SEM images were acquired to confirm the shape of materials. Figure 4 displays the FE-SEM images of the MIL-100(Fe), MIL-100(Fe)_NH_2, and MIL-100(Fe)/COF samples. The crystalline morphology of MIL-100(Fe) reveals the presence of crystals ranging in size from 200 to 800 nm. In the MIL-100(Fe)_NH_2 image, NH_2 groups bonded to the particle surfaces can be observed within the 200–800 nm size range. In the FE-SEM image of MIL-100(Fe)/COF, agglomerated crystalline particles with a uniform size of 50 nm are noticeable. Furthermore, the FE-SEM images confirms that the smooth pure MIL-100(Fe) structure significantly changes due to the loading of the COF on the MIL-100(Fe) surface. The FE-SEM images of MIL-100(Fe)/COF show that the COF is well-dispersed on the MIL-100(Fe) surface. The MIL-100(Fe)/COF surface tends to be rougher after the insertion of the COF on MIL-100(Fe) and had an effect on the MIL-100(Fe) structure.

Definitive Screening Design

Definitive screening design was employed to identify the influential factors in the synthesis of MIL-100(Fe)/COF. The precursors used in the MIL-100(Fe)/COF synthesis, namely MIL-100(Fe)_NH_2, TPA, MEL, DMSO, and DIW, were included in the definitive screening design. Table 1 presents the five factors considered, each designed with three levels. To facilitate the design process, a modified molar ratio was utilized since the molar numbers of the other four precursors were significantly larger compared to MIL-100(Fe)_NH_2. MEL and TPA were divided by 10, while DMSO and DIW were divided by 1000. For the actual synthesis, the experimental conditions were

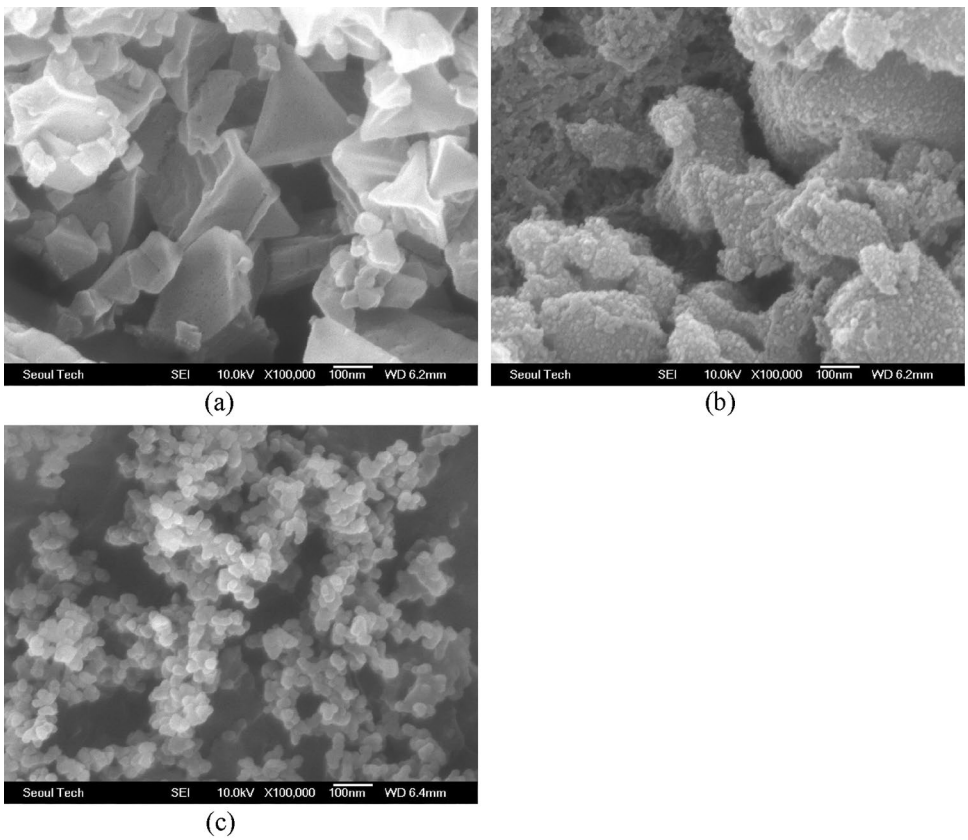

Fig. 4 FE-SEM image of **a** MOF-100(Fe), **b** MIL-100(Fe)_NH_2 and **c** MOF-100(Fe)/COF

Table 1 Factor and level for definitive screening design

Factor	Level		
	Low	Middle	High
Fe–MOF–NH_2	0.1 g	0.2 g	0.3 g
Terephthalaldehyde	0.3 g	0.5 g	0.7 g
Melamine	0.3 g	0.5 g	0.7 g
Dimethylsulfoxide	15 mL	25 mL	35 mL
Distilled water	3 mL	5 mL	7 mL

determined by multiplying the design values by the respective divided numbers. The definitive screening design was executed based on the modified molar ratios within the range specified in Table 1. This design resulted in 13 different experimental conditions. The synthesis of MIL-100(Fe)/COF was conducted at a constant reaction temperature of 180 °C for 12 h, adhering to the strain molar ratios derived from the design.

To assess the impact of the five factors (molar ratio modifications) on the elemental nitrogen content (response), main effect plots were generated and are depicted in Fig. 5. Main effect plots are useful for examining the disparity in response means among different levels of a factor and determining the presence of a main effect when the response is influenced by varying levels of a factor. The main effect plots illustrate the response means for each level of a factor connected by a line. A non-horizontal line indicates the presence of a main effect, and the steepness of the slope indicates the magnitude of the effect. From the main effect plots in Fig. 5, it is evident that TPA has the lowest effect on the response.

Mixture Method

Mixture design approach was employed to optimize the concentration of the synthetic precursors (MEL, DMSO, and DIW) identified as the main factors in the previous screening design. MIL-100(Fe)_NH_2 and TPA were held constant at 0.1 and 0.25 g, respectively. To facilitate the experimental planning, the precursor molar ratios were modified to mitigate the differences in molarity between the precursors. DMSO and DIW were assigned modified molar ratios by dividing them by 100 and 50, respectively. During the actual synthesis, these values were multiplied by the respective divided numbers. An extreme vertices design (EVD) methodology, which introduces additional constraints to the design to account for non-uniform precursor ratio ranges, was utilized. Not all precursor ratios have the same range, so the design ranges were determined based on the molar concentrations of the precursors and are presented in Table 2. The analysis was performed using the nitrogen concentration of the synthesized material as used in the definitive screening design. Table 3 displays the results of the statistical treatment of the mixture design using analysis of variance (ANOVA). A reliable model has an *R*-square value greater than 0.6 in the regression analysis. In this case, the calculated *R* square value was 0.693, confirming the reliability of the model. Additionally, a smaller *P* value indicates a better fit of the model. The low *P* value of 0.082 confirms the statistical significance of the regression model.

Figure 6 illustrates the trajectory of the Cox reaction, representing the effect of changing the ratio of one component while maintaining the mixture components at a constant ratio. The trajectory for DIW exhibits the steepest

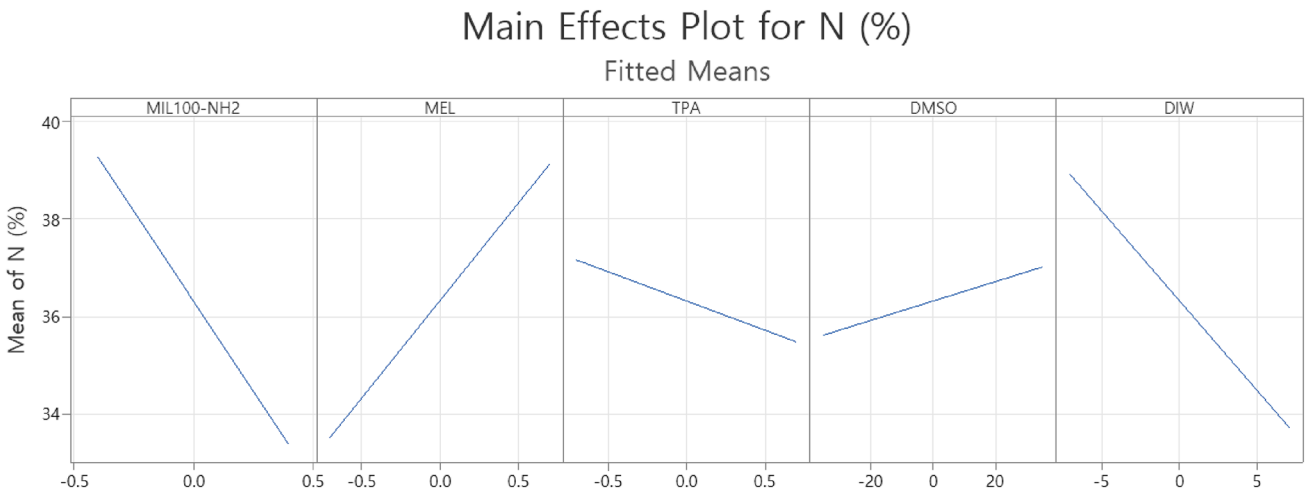

Fig. 5 Main effects plot for nitrogen contents of MOF-100(Fe)/COF synthesized with various synthesis conditions designed by definitive screening design

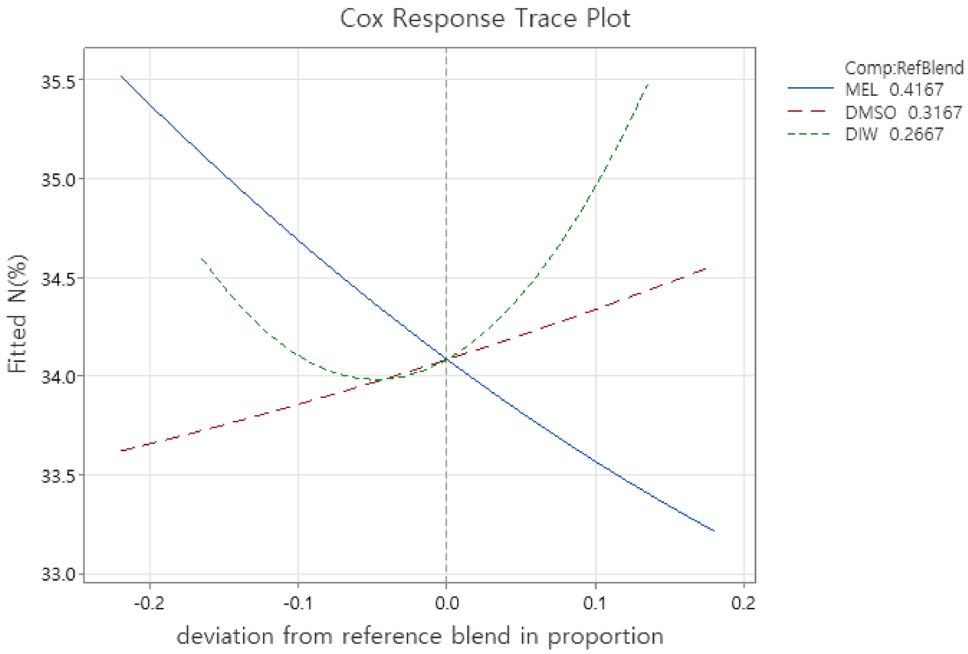

Fig. 6 Cox response trace plot of Nitrogen content of MOF-100(Fe)/COF based on precursor composition

Table 2 Bounds of mixture components for mixture design

Factor	Proportion	
	Lower	Upper
Melamine	0.2	0.6
Dimethylsulfoxide	0.1	0.5
Distilled water	0.1	0.4

and rightward slope, indicating that the strain molar ratio of DIW has the greatest impact on the reaction response. The mixture contour plots in Fig. 7 depict the nitrogen content of the MIL-100(Fe)/COF samples synthesized according to the strain molar ratio of the three main factors. A smaller MEL-to-DMSO ratio and a higher amount of DIW result in higher nitrogen content in the reaction. The optimal precursor molar ratio was predicted to be located in the lower right region of the mixture contour, suggesting that the optimal modified molar ratio for MIL-100(Fe)/COF synthesis is MEL:DMSO:DIW = 0.2:0.4:0.4. Consequently, based on this study, the estimated actual precursor ratio for the optimized synthesis of MIL-100(Fe)/COF is MIL-100(Fe)_NH_2 :TPA:MEL:DMSO:DIW = 1 mol:13 mol:10 mol:1884 mol: 1648 mol.

Methane Adsorption

Adsorption capacity measurements were conducted on 7 randomly selected adsorbents from the 13 conditions obtained from the previous mixture design to evaluate their methane adsorption performance. Figure 8 displays the mixture contour plots illustrating the adsorption capacity of the synthesized MIL-100(Fe)/COF samples at different precursor mol fractions. Surprisingly, the results obtained

Table 3 Analysis of variance (ANOVA) for mixture design

Source	DF	Seq SS	Adj SS	Adj MS	*F* value	*P* value
Model	5	6.7603	6.7603	1.3521	3.17	0.082
Linear	2	4.6444	2.7481	1.3741	3.22	0.102
Square	3	2.1159	2.1159	0.7053	1.65	0.263
MEL*DMSO	1	0.2127	0.1317	0.1317	0.31	0.596
MEL*DIW	1	0.306	1.5854	1.5854	3.71	0.095
DMSO*DIW	1	1.5973	1.5973	1.5973	3.74	0.094
Error	7	2.9874	2.9874	0.4268		
Total	12	9.7477				
R square (R^2)	0.693					

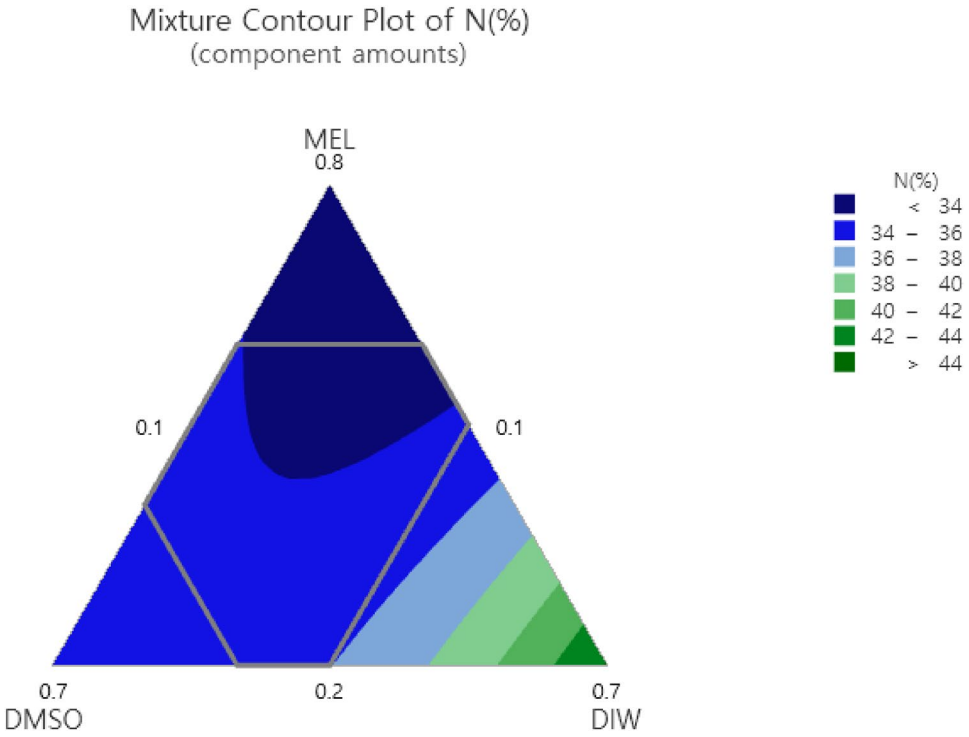

Fig. 7 Mixture contour plot of nitrogen content of MOF-100(Fe)/COF synthesized with various modified mole fraction of precursors

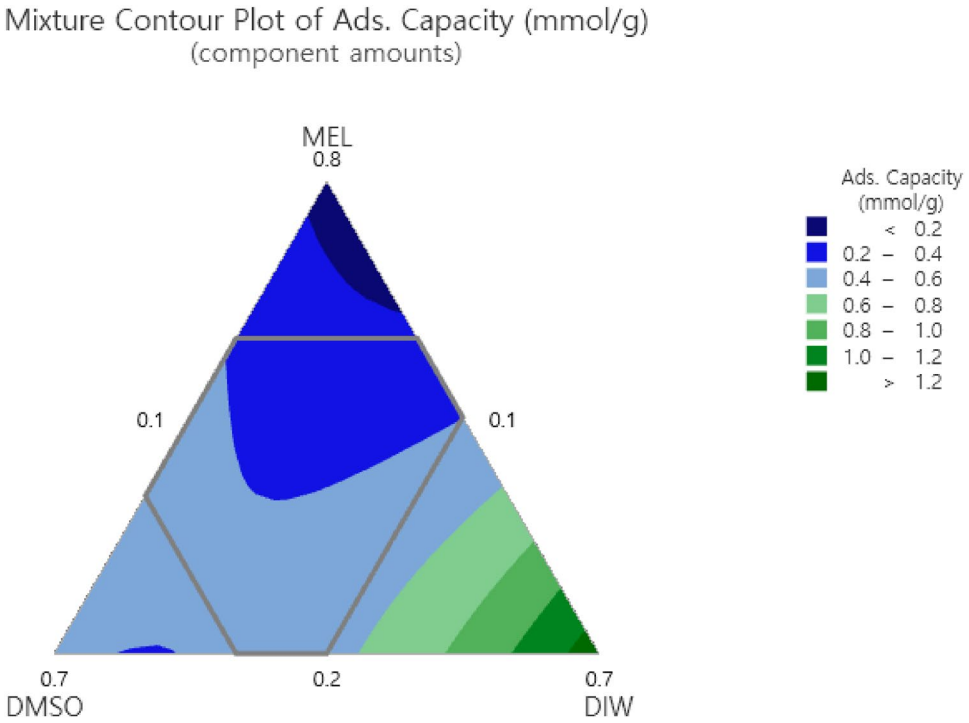

Fig. 8 Mixture contour plot of methane adsorption capacity of MOF-100(Fe)/COF synthesized with various modified mole fraction of precursors. The adsorption experiments are performed at 1 atm and 25 °C

from methane adsorption capacity and nitrogen content were remarkably similar. In fact, the correlation between the two datasets was calculated, resulting in an *R*-squared value of 0.91. This indicates that analyzing the nitrogen concentration of the adsorbents can predict their adsorption capacity using the experimental design method, eliminating the need for actual adsorption experiments. The methane adsorption was carried out at 3 atm under the same conditions to investigate the effect of adsorption performance over different adsorption conditions. The adsorption capacity increased

by 34% on average compared to that performed at 1 atm. However, the trend of the adsorption capacity for the ratio of the three components was almost similar (not shown). The optimum molar ratio for MIL-100(Fe)/COF synthesis was determined using the response optimizer tool, which demonstrates the influence of different experimental settings on the predicted responses. The response optimizer indicated that MIL-100(Fe)/COF synthesized with a modified molar ratio of 0.1:0.4:0.5 was expected to exhibit the highest value, aligning with the predicted value based on nitrogen analysis.

Conclusions

In conclusion, the field of methane adsorption has garnered significant attention due to its importance in energy storage, natural gas purification, and environmental sustainability. The development of efficient and selective adsorption materials is crucial for the storage and utilization of methane. Among the various materials investigated, metal–organic frameworks and covalent organic frameworks have emerged as promising candidates for methane adsorption. In particular, Fe-MOFs, a subset of MOFs, exhibit desirable properties such as high porosity, tunable pore size, and exceptional stability, making them highly attractive for gas storage and separation applications. However, the synthesis of MIL-100(Fe)/COF materials has traditionally relied on trial-and-error methods, which can be time-consuming and inefficient. This study addresses this limitation by employing statistical design of experiments to optimize the synthesis of MIL-100(Fe)/COF materials. Two DOE methods, screening and mixture, were utilized to identify significant precursors and optimize precursor ratios, streamlining the synthesis process. The resulting MIL-100(Fe)/COF materials were characterized using X-ray diffraction and Fourier transform infrared spectroscopy to assess their structural and chemical properties. Furthermore, methane adsorption experiments were conducted to validate the effectiveness of the optimized synthesis approach. For methane adsorption, the optimal MEL:DMSO:DIW ratio for MIL-100(Fe)/COF is 0.1:0.4:0.5. The successful optimization of MIL-100(Fe)/COF synthesis demonstrated in this study holds great promise for their widespread application as valuable adsorbents in various industries, such as energy storage, natural gas purification, and environmental remediation. Overall, the integration of statistical DOE methods with the synthesis of MIL-100(Fe)/COF materials represents a significant advancement in the field, offering a more systematic and efficient approach for the development of adsorption materials. The enhanced performance and controllability achieved through this optimization process pave the way for further advancements in methane adsorption and utilization, contributing to the sustainable energy and environmental landscape.

Acknowledgements This study was supported by the Research Program funded by the SeoulTech (Seoul National University of Science and Technology).

References

1. T.A. Makal, J.R. Li, W. Lu, H.C. Zhou, Chem. Soc. Rev. **41**, 7761 (2012)
2. I. Men'shchikov, A. Shkolin, E. Khozina, A. Fomkin, Nanomaterials **10**, 1379 (2020)
3. M. Beckner, A. Dailly, Appl. Energy **162**, 506 (2016)
4. S. Biloe, V. Goetz, S. Mauran, Carbon **39**, 1653 (2001)
5. Y. He, W. Zhou, G. Qian, B. Chen, Chem. Soc. Rev. **43**, 5657 (2014)
6. A.C. Kizzie, A. Dailly, L. Perry, M.A. Lail, W. Lu, T.O. Nelson, M. Cai, H.-C. Zhou, Mater. Sci. Appl. **5**, 8 (2014)
7. E.A. Müller, F.R. Hung, K.E. Gubbins, Langmuir **16**, 5418 (2000)
8. C.A. Grande, R. Blom, Energy Fuels **28**, 6688 (2014)
9. X. Xu, X. Zhao, L. Sun, X. Liu, J. Nat. Gas Chem. **17**, 391 (2008)
10. O.M. Yaghi, M. O'Keeffe, N.W. Ockwig, H.K. Chae, M. Eddaoudi, J. Kim, Nature **423**, 705 (2003)
11. N. Stock, S. Biswas, Chem. Rev. **1122**, 933 (2012)
12. Z. Wang, S.M. Cohen, Chem. Soc. Rev. **38**, 1315 (2009)
13. Y. Zhong, W. Liu, C. Rao, B. Li, X. Wang, D. Liu, Y. Pan, J. Liu, Curr. Med. Chem. **28**, 6179 (2021)
14. X. Zhang, Q. Liu, X. Shi, A.M. Asiri, X. Sun, Inorg. Chem. Front. **5**, 1405 (2018)
15. J. Wu, Y. Gao, S. Wei, P. Chen, D. Gu, B. Fu, M. Chen, J. Solid State Chem. **302**, 122350 (2021)
16. G. Férey, C. Mellot-Draznieks, C. Serre, F. Millange, J. Dutour, S. Surblé, I. Margiolaki, Science **309**, 2040 (2005)
17. P. Horcajada, C. Serre, M. Vallet-Regi, M. Sebban, F. Taulelle, G. Férey, M.B. Anglès d'Auriac. Angew Chem. Int. Ed. **45**, 5974 (2006)
18. F. Zhang, J. Shi, Y. Jin, Y. Fu, Y. Zhong, W. Zhu, Chem. Eng. J. **259**, 183 (2015)
19. A. López-Magano, A. Jiménez-Almarza, J. Jose Alemán, R. Mas-Ballesté, Catalysts **10**, 720 (2020)
20. H.C. Zhou, J.R. Long, O.M. Yaghi, Chem. Rev. **112**, 673 (2012)
21. H. Furukawa, K.E. Cordova, M. O'Keeffe, O.M. Yaghi, Science **341,** 1230444 (2013)
22. J.L.C. Rowsell, O.M. Yaghi, Microporous Mesoporous Mater. **73**, 3 (2004)
23. S. Kitagawa, R. Kitaura, S. Noro, Angew. Chem. Int. Ed. **43**, 2334–2375 (2004)
24. C.S. Diercks, O.M. Yaghi, Science, **355**, eaal1585 (2017)
25. X. Feng, X. Ding, D. Jiang, Chem. Soc. Rev. **41**, 6010–6022 (2012)
26. J. Li, J. Sculley, H.C. Zhou, Chem. Rev. **112**, 869–932 (2012)
27. A.P. Côté, A.I. Benin, N.W. Ockwig, M. O'Keeffe, A.J. Matzger, O.M. Yaghi, Science **310**, 1166–1170 (2005)
28. O.K. Farha, J.T. Hupp, Acc. Chem. Res. **43**, 1166–1175 (2010)
29. L.E. Kreno, K. Leong, O.K. Farha, M. Allendorf, Van R.P. Duyne, J.T. Hupp, Chem. Rev. **112**, 1105–1125 (2012)

30. R.N. Kackar, J. Qual. Technol. **17**, 176 (1985)
31. K. Papadopoulou, V. Dimitropoulos, F. Rigas, Environ. Prog. Sustain. Energy **34**, 1705 (2015)
32. S. Ranganathan, J. Tebbe, L.O. Wiemann, V. Sieber, Process. Biochem. **51**, 1479 (2016)
33. M. Roosta, M. Ghaedi, A. Daneshfar, R. Sahraei, Spectrochim. Acta A **122**, 223 (2014)
34. M. Ghaedi, E. Alam Barakat, A. Asfaram, B. Mirtamizdoust, A.A. Bazrafshan, S. Hajati, RSC Adv. **5**, 42376 (2015)
35. G. Chaturvedi, A. Kaur, A. Umar, M.A. Khan, H. Algarni, S.K. Kansal, J. Solid State Chem. **281**, 121029 (2020)
36. M. Firoozi, Z. Rafiee, K. Dashtian, ACS Omega **5**, 9420 (2020)
37. J.S. Eensalu, K. Tõnsuaadu, J. Adamson, I.O. Acik, M. Krunks, J. Therm. Anal. Calorim. **147**, 4899 (2022)